Exacerbated heat stress induced by urban browning in the Global South

Article *in* Nature Cities · January 2025

DOI: 10.1038/s44284-024-00184-9

17 authors, including:

Du Huilin
Nanjing University
27 PUBLICATIONS **403** CITATIONS
SEE PROFILE

Wenfeng Zhan
Nanjing University
156 PUBLICATIONS **5,146** CITATIONS
SEE PROFILE

Bing-Bing Zhou
Ocean University of China
34 PUBLICATIONS **1,053** CITATIONS
SEE PROFILE

Yang Ju
Nanjing University
38 PUBLICATIONS **595** CITATIONS
SEE PROFILE

nature cities

Article

https://doi.org/10.1038/s44284-024-00184-9

Exacerbated heat stress induced by urban browning in the Global South

Received: 14 May 2024

Accepted: 14 November 2024

Published online: 06 January 2025

Check for updates

Huilin Du[1], Wenfeng Zhan[1,2,3] ✉, Bingbing Zhou[4], Yang Ju[5], Zihan Liu[6], Ariane Middel[7], Kangning Huang[8], Lei Zhao[9], TC Chakraborty[10], Zhihua Wang[11], Shasha Wang[1], Jiufeng Li[1], Long Li[1], Fan Huang[12], Yingying Ji[1], Xuecao Li[13] & Manchun Li[5] ✉

Cities in the Global South face dual pressures from intensifying heat stress and widespread urban browning. However, the specific trends in urban heat stress across these cities, alongside those induced by urban browning, remain inadequately quantified, hampering effective urban planning and intervention strategies. Here we present a data-driven methodology to generate high-resolution (1 km) summertime Heat Index (HI) maps for over 2,300 Global South cities (2003–2020). This dataset recalibrates HI-based warming rates, revealing a mean trend (K_{HI}) of 0.41 ± 0.01 °C per decade (mean ± standard error) across these cities. Urban browning exacerbates heat stress significantly, with K_{HI} increases surpassing 0.05 °C per decade in cities such as those in Nigeria, contrasting starkly with greening-induced cooling observed in many Global North cities. Our analysis pinpoints cities in dire need of intervention, such as those in Botswana and Côte d'Ivoire facing browning-driven HI increases without commensurate economic growth. Contrastingly, Chinese and Indian cities exhibit a paradoxical cooling trend, potentially linked to greening initiatives amid economic development. Our findings highlight key action imperatives for South–South knowledge exchange to develop targeted governance strategies for achieving urban sustainability.

More than 75% of the world's urban population currently resides in the Global South, a region anticipated to witness nearly 96% of future urban population growth by 2050 (ref. 1). In this regard, a critical challenge to urban sustainability stands out—the compounding effects of rising temperature and humidity are pushing urban moist heat stress to critical human tolerance thresholds[2–5]. This challenge is compounded by the relatively underdeveloped socio-economic and infrastructural conditions in these regions[6,7]. Unlike the Global North, urban browning (that is, widespread vegetation loss) is prevalent across most Global South cities[8], leading to exacerbated heat stress and associated health risks[3,9]. To foster climate-resilient and sustainable urban development, it is imperative to accurately monitor and strategically address urban heat stress trends induced by vegetation change over these rapidly urbanizing areas.

Across the Global South, conventional urban heat stress assessments have predominantly relied on in situ surface air temperature (SAT) data obtained from monitoring stations in selected cities[10–12].

[1]Jiangsu Provincial Key Laboratory of Geographic Information Science and Technology, International Institute for Earth System Science, Nanjing University, Nanjing, China. [2]Jiangsu Center for Collaborative Innovation in Geographical Information Resource Development and Application, Nanjing, China. [3] Frontiers Science Center for Critical Earth Material Cycling, Nanjing University, Nanjing, China. [4]School of International Affairs and Public Administration, Ocean University of China, Qingdao, China. [5]School of Geography and Ocean Science, Nanjing University, Nanjing, China. [6]School of Artificial Intelligence, Anhui University, Hefei, China. [7]Global Institute of Sustainability and Innovation, Arizona State University, Tempe, AZ, USA. [8]New York University Shanghai, Shanghai, China. [9]Department of Civil and Environmental Engineering, University of Illinois at Urbana-Champaign, Urbana, IL, USA. [10]Atmospheric Sciences and Global Change Division, Pacific Northwest National Laboratory, Richland, WA, USA. [11]School of Sustainable Engineering and the Built Environment, Arizona State University, Tempe, AZ, USA. [12]College of Geography and Remote Sensing, Hohai University, Nanjing, China. [13]College of Land Science and Technology, China Agricultural University, Beijing, China. ✉e-mail: zhanwenfeng@nju.edu.cn; nju_mycs@163.com

https://doi.org/10.1038/s44284-024-00184-9

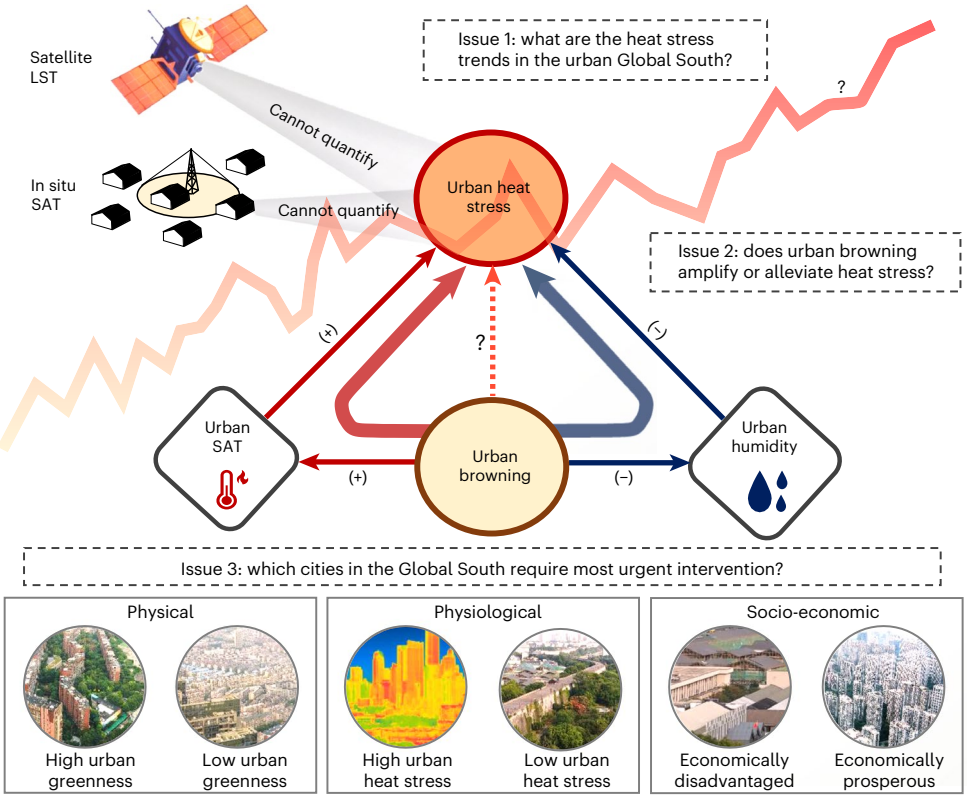

Fig. 1 | Three interconnected issues regarding browning-induced urban heating across the Global South cities. Satellite-based LST and sparse in situ SAT both cannot accurately characterize urban heat stress, leading to uncertainties in heat stress trends in the urban Global South (Issue 1). Vegetation loss has two opposite effects on heat stress—it amplifies heat stress by elevating temperature (represented by '+') and alleviates it by reducing absolute humidity (denoted by '−'). This dual urban climate response to vegetation loss highlights a critical knowledge gap, particularly for the urban Global South (Issue 2). Furthermore, the complex interplay of multiple city-level characteristics (including physical, physiological and socio-economic factors) in modulating heat stress makes it challenging to identify cities for the most urgently requiring interventions (Issue 3).

In situ SAT data have also been integrated with humidity information to assess moist heat trends for a limited subset of Global South cities[13]. Unfortunately, most Global South cities have a scarce weather station network or lack monitoring infrastructure entirely (Supplementary Fig. 1). This data scarcity, compounded by the inherent heterogeneity of urban landscapes, hinders the accurate monitoring of heat stress trends over this vast region. In contrast to the limited availability of SAT from ground-based stations, satellite-derived land surface temperature (LST) data offer thermal observations with extensive spatio-temporal coverage[14]. Recent investigations have revealed that the LST-based warming rate in Global South cities can reach up to 0.5 °C per decade[15–17]. Importantly, the warming rate is not uniform—more pronounced in urban peripheries compared to urban cores[15] and in cities with higher economic levels[16]. The presence of variations in urban browning (or the opposite, urban greening) introduces an additional layer of complexity. Satellite observations suggest a marginal greening trend in most Asian cities, particularly those in China[18], which has reduced LST-based urban warming[15,19]. Conversely, numerous cities in Africa and South America have witnessed substantial urban browning[8], exacerbating LST-based warming[15]. The phenomenon of browning-induced warming is particularly prevalent in economically disadvantaged cities within South America[16].

Three issues impede our understanding and interventions of urban heating across the Global South (Fig. 1). First, satellite thermal data often inadequately characterize heat stress[20–22]. Similarly, heat estimates from sparse in situ observations (Supplementary Fig. 1) or coarse-resolution reanalysis data[23] frequently fail to capture the heterogeneous urban environment and the experienced actual outdoor heat. Integration of these diverse datasets has been commendably utilized to generate urban moist heat profiles[5,24]. Nonetheless, their relatively coarse spatial resolution (approximately 5 km) presents a challenge in accurately capturing fine-scale intra-city heat stress trends, particularly in medium- and small-sized cities. As a result, high-resolution trends in physiologically relevant urban warming remain largely unknown across the Global South. Second, vegetation loss and degradation, as a consequence of urbanization, not only elevates urban air temperature but also reduces humidity[20,25]. The net impacts of vegetation loss and degradation on heat stress trends remain unclear across diverse Global South cities. Third, whereas case studies underscore the importance of socio-economic factors in prioritizing urban greening strategies[16], existing frameworks remain insufficient for identifying Global South cities that warrant the most urgent intervention due to the intricate interplay among physical, physiological and socio-economic factors. In light of these challenges, our study seeks to answer three fundamental research questions:

1. What are the prevailing trends in urban heat stress at a refined spatial resolution across Global South cities, and how do these trends diverge from urban heating trends derived from LST and SAT data?
2. To what extent does urban browning in Global South cities modulate urban heat stress, and what are the underlying spatio-temporal dynamics?
3. Which cities in the Global South should be prioritized for intervention to mitigate heat stress induced by urban browning, considering the economic and technological constraints specific to the Global South?

Here we developed a unique, fine-resolution (1-km) summertime urban Heat Index (HI) dataset for over 2,300 Global South cities from

https://doi.org/10.1038/s44284-024-00184-9

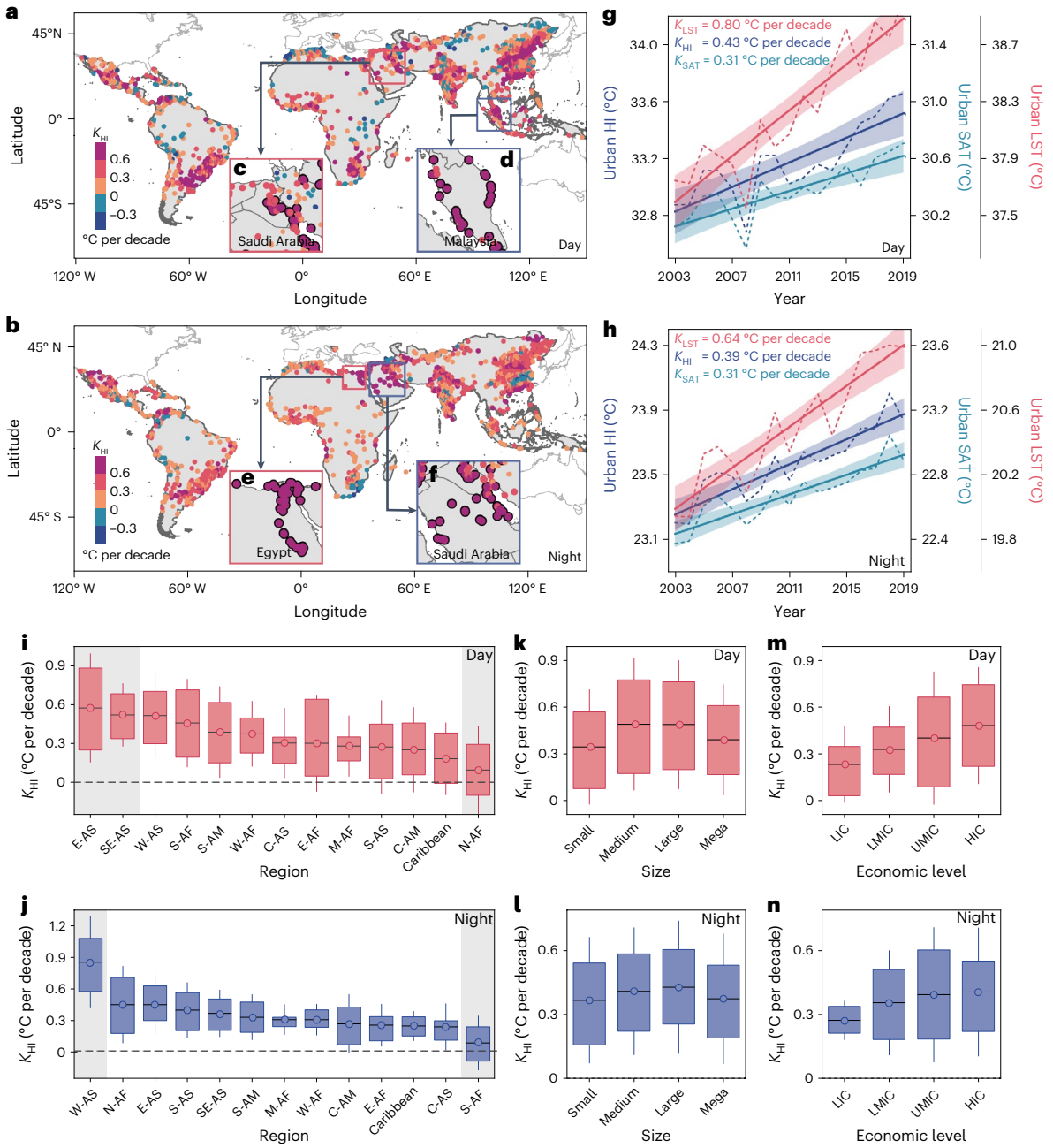

Fig. 2 | Summertime urban heat stress trends in 2,341 Global South cities between 2003 and 2020. a,**b**, Spatio-temporal patterns of K_{HI} for daytime (**a**) and nighttime (**b**). **c**–**f**, Zooming into typical regions, including Saudi Arabia (**c**) and Malaysia (**d**) for daytime, and Egypt (**e**) and Saudi Arabia (**f**) for nighttime. **g**,**h**, Year-to-year variations of urban HI, SAT and LST (represented by dashed lines), along with their trend lines (depicted by solid lines) for daytime (**g**) and nighttime (**h**), with shading indicating 95% confidence intervals. **i**,**j**, Boxplots depicting daytime (**i**) and nighttime (**j**) K_{HI} in cities within various subcontinents, with abbreviations representing various regions: SE-AS (southeastern Asia; with the city sample size of 118), S-AS (southern Asia; 288 cities), W-AS (western Asia; 88 cities), E-AS (eastern Asia; 902 cities), C-AS (central Asia; 64 cities), W-AF (western Africa; 80 cities), S-AF (southern Africa; 117 cities), N-AF (northern Africa; 142 cities), M-AF (middle Africa; 22 cities), E-AF (eastern Africa; 34 cities), Caribbean (25 cities), C-AM (Central America; 112 cities) and S-AM (South America; 336 cities). **k**,**l**, Boxplots depicting daytime (**k**) and nighttime K_{HI} (**l**) in cities characterized by different population densities, including small (<630 persons km^{-2}; 585 cities), medium (630–1,977 persons km^{-2}; 585 cities), large (1,977–4,430 persons km^{-2}; 585 cities) and megacities (>4,430 persons km^{-2}; 586 cities; Methods). **m**,**n**, Boxplots showing daytime (**m**) and nighttime (**n**) K_{HI} across cities with varying economic levels, classified as low-income (LIC; GDP per capita < US$1,045; 19 cities), low–middle income (LMIC; US$1,045–4,125; 184 cities), upper–middle income (UMIC; US$4,126–12,735; 1,078 cities) and high-income cities (HIC; >US$12,735; 1,012 cities). In **i** and **j**, the gray shading highlights the regions with the highest and lowest K_{HI} values. In **i**–**n**, the center line represents the mean, whereas the lower and upper lines denote 25th and 75th quantiles, respectively. The lower and upper bounds of the whiskers indicate one standard deviation (SD) below and above the mean, respectively.

2003 to 2020. We leveraged data from openly accessible in situ observations, reanalysis data and remote sensing products and employed data-driven spatio-temporal estimation models to enhance accuracy. On the basis of these datasets, we conducted a comprehensive analysis of urban heat stress trends (K_{HI}) and quantified the impact of urban browning on these trends (β_{HI}). Subsequently, we identified priority cities/countries for intervention by considering the complex interplay between physical, physiological and socio-economic factors. Our study

offers methodologies and actionable insights for developing targeted and effective strategies to address urban heat risks, fostering climate-resilient and more sustainable urban development in the Global South.

Results

Urban heat stress trends across the Global South

We generated summertime urban HI datasets at 1-km resolution for Global South cities between 2003 and 2020, employing a spatio-temporal estimation model that integrates multi-source data with a random forest algorithm (Supplementary Fig. 2 and Methods). Through cross-validation with ground-based measurements, we demonstrated the robust performance of the generated urban HI datasets (R = 0.98 for both daytime and nighttime) and the derived interannual trends (R = 0.82 and 0.74 for daytime and nighttime, respectively; Supplementary Note 1). Our sensitivity analysis indicates minimal influence of estimation errors in urban HI on the derived K_{HI}, contributing to an uncertainty of only ~5% (Supplementary Note 1). Moreover, our datasets exhibit resilience to variations in location and the number of urban stations employed for HI estimation (Supplementary Note 2).

Utilizing this high-quality dataset, we examined the spatio-temporal trends in urban HI (K_{HI}) across two distinct urban zones: urban cores (urbanized areas before year 2000) and urban transition zones (urbanized areas after year 2000; Methods). Our analysis reveals that nearly 90% of Global South cities experience a significant positive K_{HI} (Fig. 2a,b). Urban cores exhibit an average daytime K_{HI} of 0.43 ± 0.01 °C per decade (mean ± standard error), and this trend translates into 0.39 ± 0.01 °C per decade at night (Fig. 2g,h). These trends correspond to a 2.4% increase in the average day–night urban HI from 2003 to 2020. Such a sustained HI increase could substantially elevate the number of cities categorized as 'Danger' according to NOAA's risk categorization (Discussion and implications). Moreover, these HI-based urban heat stress trends slightly exceed those derived from SAT (0.31 ± 0.01 °C per decade for both day and night; Fig. 2g,h and Supplementary Fig. 3c,d), but are notably lower than the estimates based on satellite-derived LST (0.80 ± 0.02 °C per decade for daytime and 0.64 ± 0.01 °C per decade for nighttime; Fig. 2g,h and Supplementary Fig. 3a,b). Interestingly, the spatio-temporal patterns and magnitudes of K_{HI} in urban transitional zones closely resemble those in urban cores (Supplementary Fig. 4). This deviates from LST-based studies suggesting that warming rates in urban transition zones nearly double those of urban cores[15]. The difference between HI and LST responses to urbanization may underlie the contrasting warming patterns. LST-based warming manifests the direct impact of reduced evapotranspiration following vegetation removal during urbanization. By comparison, HI incorporates both temperature and humidity—reduced evapotranspiration increases SAT indirectly through complex surface–atmosphere interactions, yet it also decreases humidity, thereby mitigating the impacts of vegetation loss on HI[20]. To supplement the analysis relying on HI, we employed alterative heat stress metrics, including the Humidex and Wet-Bulb Globe Temperature in shade conditions at stable wind (termed indoor WBGT), to assess potential discrepancies due to variations in humidity contributions to heat stress metrics[26]. All these metrics exhibit consistent spatial patterns, reinforcing the robustness of our findings (Supplementary Note 3).

The daytime and nighttime K_{HI} in Global South cities reveal substantial variations across continents and countries (Fig. 2i,j). Eastern and southeastern Asian cities exhibit relatively high daytime K_{HI} (0.57 ± 0.01 °C per decade and 0.52 ± 0.02 °C per decade, respectively), whereas northern African cities possess modest daytime K_{HI} (0.09 ± 0.03 °C per decade; Fig. 2i). At night, the highest K_{HI} of 0.85 ± 0.05 °C per decade is observed in western Asian cities, whereas southern African cities demonstrate a marginal K_{HI} (0.08 ± 0.02 °C per decade; Fig. 2j). These geographical variations in K_{HI} are jointed regulated by background climate change, urbanization processes and changes in urban greenness (Supplementary Fig. 5). For instance, the marked divergence in K_{HI} patterns between daytime and nighttime observed in numerous Southern African cities—positive during the day but negative at night (Fig. 2a,b)—closely mirrors those of their rural backgrounds (Supplementary Fig. 6e,f), probably suggesting a strong influence from background climate changes. Among the countries, daytime K_{HI} is most prominent in cities of Malaysia (0.70 ± 0.03 °C per decade) and Turkmenistan (0.64 ± 0.08 °C per decade; Fig. 2 and Supplementary Fig. 7a–d). Nighttime K_{HI} paints a marginally different picture, with cities in the Middle East, particularly Saudi Arabia (1.10 ± 0.06 °C per decade) and Egypt (0.97 ± 0.02 °C per decade), demonstrating the most rapid heat stress trends (Fig. 2 and Supplementary Fig. 7e–h).

Our analysis unveils an uneven distribution of K_{HI} across Global South cities concerning population density and economic status (Fig. 2k–n). Notably, both daytime and nighttime K_{HI} first increase and then decrease with urban population density (Fig. 2k,l). Regarding economic status, both daytime and nighttime K_{HI} tend to be higher in economically prosperous cities (Fig. 2m,n). For example, the daytime K_{HI} steadily increases from 0.23 ± 0.05 °C per decade in low-income cities to 0.48 ± 0.01 °C per decade in high-income cities (Fig. 2m). This finding resonates with prior research in Latin America, which linked LST-based urban heating rates to economic status[16]. Cities with higher economic levels often undergo more pronounced vegetation loss during early phases of urbanization driven by economic development, probably contributing to their observed faster urban heating rates[16].

Urban browning-induced heat stress trends

Between 2003 and 2020, Global South cities witness widespread browning in both urban cores (K_{EVI} = −0.007 ± 0.0004 per decade, corresponding to a 5% decrease in enhanced vegetation index (EVI)) and urban transition zones (K_{EVI} = −0.016 ± 0.0005 per decade, that is, a 9% decrease in EVI; Supplementary Figs. 8 and 9), presenting a striking divergence from the prevailing urban greening observed in Global North cities (0.003 ± 0.0002 per decade for urban cores and 0.001 ± 0.0002 per decade for urban transition zones). To isolate the impacts of urban browning on K_{HI} (denoted as β_{HI}) in Global South cities, we employed the widely established least squares statistical attribution method[15,27,28]. Our results show that on average, across the urban cores of Global South, β_{HI} is about 0.022 ± 0.002 °C per decade during both daytime and nighttime (Fig. 3a,b), suggesting the dominance of browning-induced warming effect over its drying influence (Supplementary Fig. 10). Whereas the average β_{HI} may appear modest, it masks substantial spatial variations. Notably, cities in Nigeria, Botswana and Malaysia record the highest daytime mean β_{HI} values, exceeding 0.05 °C per decade (Fig. 3a). This could translate to a surge in the frequency of extreme heat days experienced by urban residents (Discussion and implications). In contrast, the prevailing urban greening phenomenon in Global North cities has attenuated urban heat stress trends by approximately 0.007 ± 0.001 °C per decade during both daytime and nighttime (Supplementary Fig. 11).

We observe a heterogeneous distribution of β_{HI} across cities in different continents and with varying population densities and economic status (Fig. 3). Among continents (Fig. 3g,h), daytime β_{HI} peaks in western African cities (0.07 ± 0.008 °C/ per decade) while registering the lowest in eastern Asian cities (about 0.01 ± 0.003 °C per decade; Fig. 3g). At night, southern Asian cities exhibit the highest β_{HI} (0.05 ± 0.006 °C per decade), whereas Caribbean and eastern Asian cities demonstrate marginal β_{HI} values (0.009 ± 0.015 °C per decade and 0.004 ± 0.003 °C per decade, respectively; Fig. 3h). The spatial disparities of β_{HI} in the urban Global South are associated with the spatial patterns observed in their corresponding K_{EVI}—for example, western African cities showcase the most pronounced browning (Supplementary Fig. 9a,b), probably explaining their high β_{HI}. Our results show that both daytime and nighttime β_{HI} generally increase with urban population density, though with a slight decrease in megacities

https://doi.org/10.1038/s44284-024-00184-9

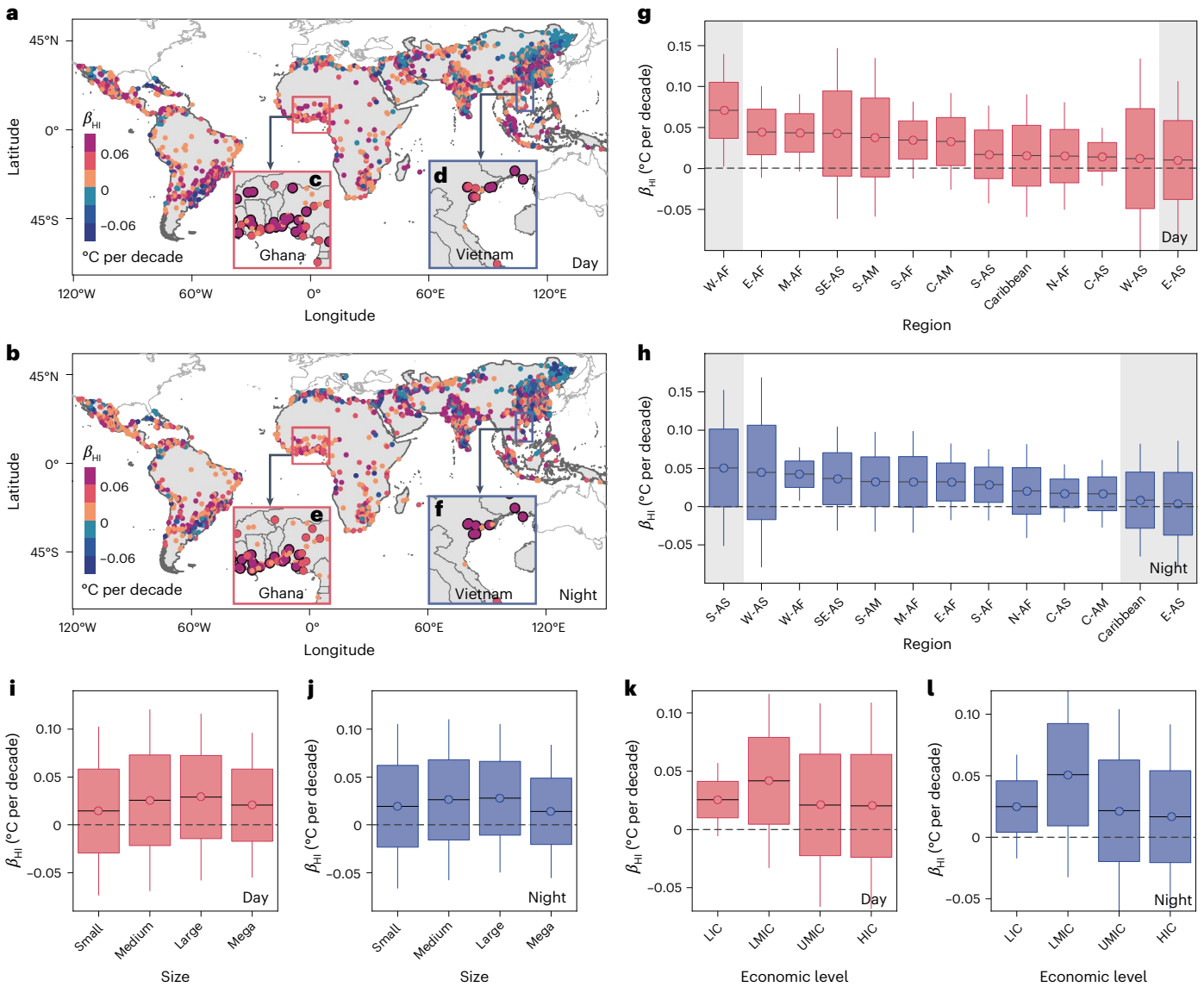

Fig. 3 | Urban browning-induced K_{HI} in Global South cities. a–**f**, Spatial distribution of daytime (**a**) and nighttime (**b**) β_{HI} and detailed enlargements in selected typical regions, including Ghana (**c**) and Vietnam (**d**) for daytime, and Ghana (**e**) and Vietnam (**f**) for nighttime. **g**,**h**, Boxplots representing the variations of daytime (**g**) and nighttime (**h**) β_{HI} across cities in different subcontinents, with abbreviations representing various regions: SE-AS (southeastern Asia; with the city sample size of 118), S-AS (southern Asia; 288 cities), W-AS (western Asia; 88 cities), E-AS (eastern Asia; 902 cities), C-AS (central Asia; 64 cities), W-AF (western Africa; 80 cities), S-AF (southern Africa; 117 cities), N-AF (northern Africa; 142 cities), M-AF (middle Africa; 22 cities), E-AF (eastern Africa; 34 cities), Caribbean (25 cities), C-AM (Central America; 112 cities) and S-AM (South America; 336 cities). **i**,**j**, Boxplots illustrating the distribution of daytime (**i**) and nighttime (**j**) β_{HI} in cities characterized by different population densities, including small (585 cities), medium (585 cities), large (585 cities) and megacities (586 cities). **k**,**l**, Boxplots depicting daytime (**k**) and nighttime (**l**) β_{HI} across cities with varying economic levels, categorized as low-income (LIC; 19 cities), low–middle income (LMIC; 184 cities), upper–middle income (UMIC; 1,078 cities) and high-income cities (HIC; 1,012 cities). In **g** and **h**, the gray shading highlights the regions with the highest and lowest β_{HI} values. In subplots **g**–**l**, the center line represents the mean, whereas the lower and upper lines denote 25th and 75th quantiles, respectively. The lower and upper bounds of the whiskers indicate one SD below and above the mean, respectively.

(Fig. 3i,j). Cities with higher population densities are typically associated with more extensive urbanization, leading to more pronounced browning and, consequently, a larger β_{HI}. Whereas in megacities with very high population densities, urbanization may stabilize, prompting increased investment in green infrastructure and thus resulting in a slightly reduced β_{HI}. Regarding economic status, daytime β_{HI} is greater in cities with low and lower–middle income levels (0.026 ± 0.007 °C per decade and 0.042 ± 0.005 °C per decade, respectively) than in those with upper–middle and high-income levels (0.021 ± 0.003 °C per decade and 0.020 ± 0.003 °C per decade, respectively; Fig. 3k). Similar patterns are also observed at night (Fig. 3l). Unlike economically prosperous cities with relatively stable urbanization, cities striving for economic advancement (typically those with low and lower–middle income levels) often undergo extensive urbanization. This extensive urbanization is often accompanied by converting natural or vegetation surfaces to impervious surfaces[29], significantly amplifying the K_{HI} induced by urban browning.

Global South cities requiring urgent interventions

We investigated city- and country-level relationships between β_{HI} and critical physical, physiological and socio-economic factors to identify specific Global South cities in dire need of interventions against browning-induced heat stress (Fig. 4). These factors include the urban greenness trend (that is, K_{EVI}; physical perspective), the absolute magnitude

https://doi.org/10.1038/s44284-024-00184-9

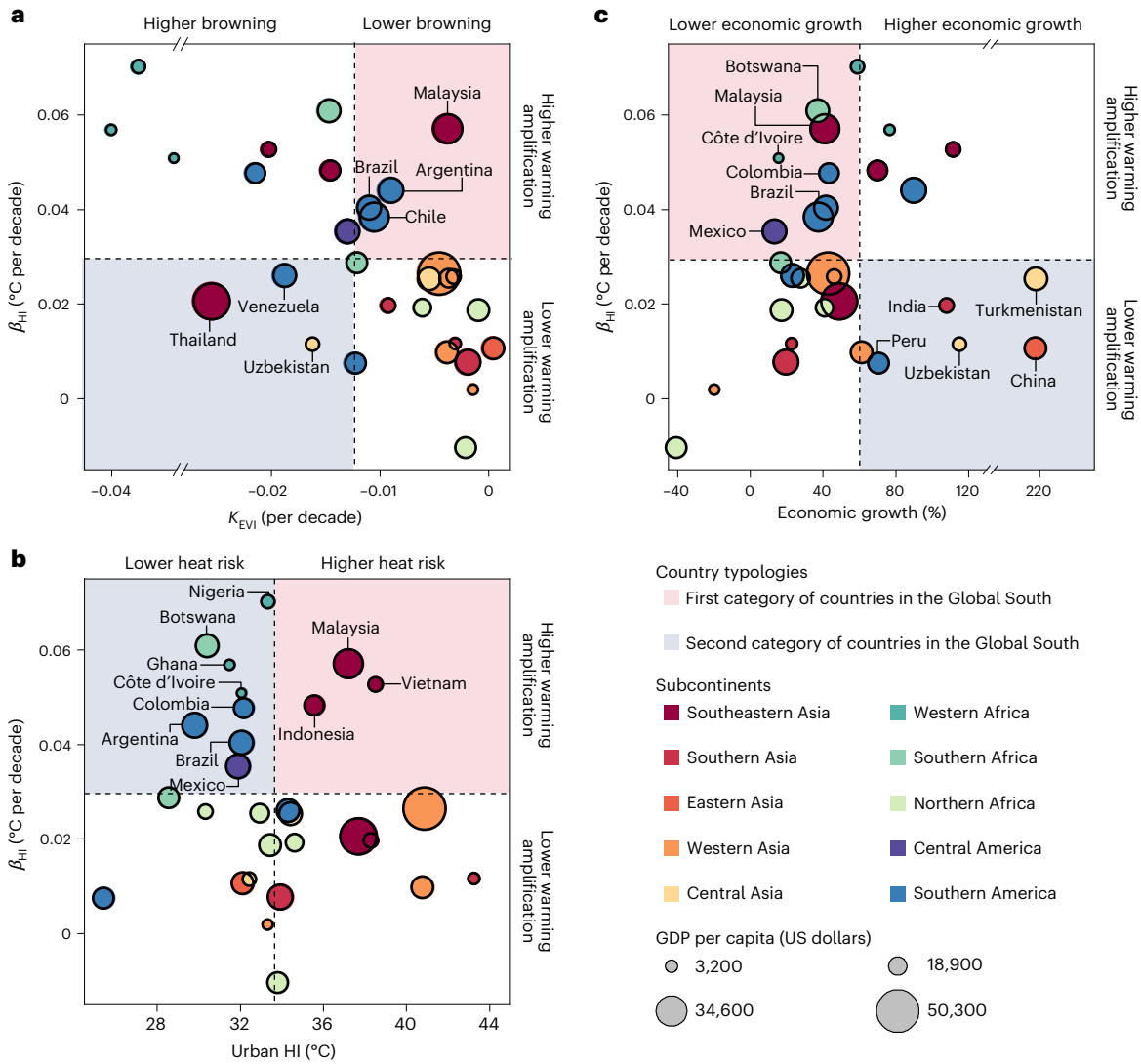

Fig. 4 | Interplay of browning-induced urban heat stress trends with urban greenness trend, HI and economic growth during summer daytime across Global South cities, through a three-part typology of countries. a–**c**, Four-quadrant plots showing β_{HI} versus K_{EVI} (**a**; physical perspective), β_{HI} versus urban HI (**b**; physiological perspective) and β_{HI} versus urban economic growth (**c**; socio-economic perspective) across Global South countries, with the quadrant thresholds (that is, dashed lines) defined by the mean value of each indicator across all countries (Supplementary Tables 1–3). Each perspective specifically delineates two distinct subcategories of countries. **a**, Physical perspective, contrasting countries with lower K_{EVI} yet relatively higher β_{HI} (pink rectangle) and those with higher K_{EVI} but relatively lower β_{HI} (blue rectangle). **b**, Physiological perspective, distinguishing countries with both higher β_{HI} and urban HI values (pink rectangle) versus those with higher β_{HI} yet lower urban HI values (blue rectangle). **c**, Socio-economic perspective, identifying countries with sluggish economic growth but higher β_{HI} (pink rectangle) and those with rapid economic growth alongside comparatively modest β_{HI} (blue rectangle). The *x*-axis breaks in **a** and **c** are used to avoid large blank spaces, making the presented data more compact.

of urban heat stress (that is, urban HI, measured by the multi-year average of HI throughout the study period; physiological perspective) and the urban economic growth (measured by the percentage increase in Gross Domestic Product (GDP) per capita throughout the study period; socio-economic perspective; Methods). To achieve this, we employed four-quadrant plots of β_{HI} against each indicator, with quadrant thresholds determined by the mean values across all countries (Supplementary Tables 1–3). Our assessments demonstrate that the relationship between K_{EVI} and β_{HI} is not linear (Fig. 4a), though both metrics are well correlated with the baseline EVI (Supplementary Fig. 12). For example, higher urban browning (that is, $K_{EVI} < -0.012$ per decade; Supplementary Table 1) may be associated with lower β_{HI} values (that is, <0.030 °C per decade), as observed in Thailand, Venezuela and Uzbekistan (Fig. 4a). Conversely, lower urban browning (that is, $K_{EVI} > -0.012$ per decade) may also coincide with higher β_{HI} values (that is, >0.030 °C per decade), as manifested in cities in Malaysia, Argentina, Chile and Brazil (Fig. 4a). These observations may underscore a greater increase in HI with each unit decrease in EVI (that is, greater vegetation cooling efficiency) in these cities, highlighting an increased necessity for urban greening intervention strategies (Discussion and implications).

We reveal a stark reality wherein numerous Global South cities already grappling with high baseline heat stress are experiencing accelerated browning-induced increases in HI (Fig. 4b and Supplementary Table 2). This concerning synergy is common in cities across Southeastern Asia, such as Malaysia, Vietnam and Indonesia, where people experience not only high summer daytime HI values surpassing 33.6 °C but also pronounced β_{HI} exceeding 0.030 °C per decade (Fig. 4b). In these cities, the high β_{HI} can translate into a more substantial uptick in extreme heat days when compared to their counterparts with lower baseline HI (Discussion and implications). Although the baseline urban HI values in countries such as Ghana and Cote d'Ivoire remain moderate (<33.6 °C; Fig. 4b), these seemingly lower levels of heat stress should not

cultivate a false sense of security. On the contrary, given the higher β_{HI} in these cities (>0.030 °C per decade; Fig. 4b), along with the relative lack of preparedness and potentially inadequate adaptive capacity[30,31], exercising caution in dealing with escalating heat stress is imperative for policymakers in these cities.

Our analysis unravels a discernible correlation between browning-induced heat stress amplification (that is, β_{HI}) and economic development across Global South cities (Fig. 4c and Supplementary Table 3). Rapid urbanization associated with economic growth often involves transforming natural vegetation to impervious surfaces[32], resulting in high β_{HI}. Nevertheless, this correlation is not universal. Some cities experiencing modest economic growth (<59%) over the last two decades, such as those in Côte d'Ivoire and Colombia, manifest notable browning effects (β_{HI} > 0.030 °C per decade; Fig. 4c). In contrast, Chinese and Indian cities showcase how strategic urban planning can align economic growth with environmental preservation, maintaining relatively lower β_{HI} values amidst modernization (Fig. 4c). This is likely attributed to the proactive urban greening programs amid rapid urbanization[29,33] (Discussion and implications).

Discussion and implications

This study recalibrates urban warming rates across over 2,300 Global South cities using a newly generated fine-resolution (1-km) HI dataset, departing from previous methods mostly relying on either satellite-based LST observations or in situ SAT measurements. Our findings highlight substantial discrepancies between the trends in HI and LST/SAT (Fig. 2g,h), underscoring the inclusion of humidity when gauging changes in urban heat stress. The generated urban HI datasets, along with the devised spatio-temporal estimation model, hold promise for future studies on Global South cities, often understudied due to data scarcity[34]. Our assessments reveal an average summer HI increase of 0.66 °C across Global South cities over the past two decades, with certain major urban centers (for example, those in Saudi Arabia) experiencing even greater increases exceeding 1.70 °C (Supplementary Fig. 7). Whereas these increments may appear modest, sustained HI elevation could substantially increase the number of cities categorized as 'Danger' based on the risk categorization used by the US National Oceanic and Atmospheric Administration from human perception perspective[35]. For example, if the current HI-based warming trend persists, the proportion of 'Danger' cities across the Global South could rise from 7% to 20% by 2050. These escalating trends indicate a notable rise in urban population exposure to extreme heat waves, carrying important implications for public health and well being throughout the Global South.

Whereas prior studies have quantified the impact of vegetation loss on LST-based warming[15,16], our investigation delves further into exploring its impact on moist heat-based urban warming. In terms of moist heat-based urban warming, our analysis demonstrates that vegetation loss exerts a more pronounced warming impact through reduced evaporative cooling compared to its drying effect via a weakened water vapor source across the Global South (Fig. 3). This contrasts starkly with the prevalent greening trends observed in many Global North cities and the cooling effects they generate (Supplementary Figs. 8 and 11), underscoring another under-recognized disparity between these two regions. Beyond general recommendations for urban greening, we identify specific cities and countries requiring urgent measures to combat heat stress induced by urban browning, considering their unique biophysical and socio-economic conditions. We reveal a negative correlation between socio-economic status and HI increases resulting from vegetation loss (that is, β_{HI}; Fig. 3k,l). This indicates the shared responsibility of national and local governments to support disadvantaged cities with limited resources for urban greening programs[16]. Our study demonstrates that countries such as Nigeria, Colombia, Turkmenistan and Chile exhibit higher inequality in both daytime and nighttime β_{HI} than other countries with similar economic status (Supplementary Fig. 13 and Supplementary Note 4), underlining the urgent need for these countries to narrow inter-city disparities of β_{HI} through urban renewal or greening programs. Furthermore, our results suggest that countries such as Malaysia, Argentina, Chile and Brazil experience modest vegetation loss alongside notable heating rates (that is, higher β_{HI}; Fig. 4a), implying an elevated heat stress sensitivity to vegetation loss in these regions (that is, vegetation cooling efficiency; ref. 36). For countries with high baseline heat stress such as Malaysia (Fig. 4b), vegetation loss-induced heating (0.057 °C per decade) can lead to a considerable increase in extreme heat events (Supplementary Note 5), signifying critical significance of contextualizing these trends within specific climatic background. Economically constrained cities may benefit from cost-effective measures such as public awareness campaigns, educational resources for urban gardening and distribution of affordable seedlings to encourage local vegetation planting[37]. In contrast, wealthier cities could explore options such as green infrastructure subsidies for urban development projects and stricter land-use regulations to protect green areas[38].

Our findings highlight opportunities for knowledge exchange among Global South cities. Many African countries, such as Côte d'Ivoire and Botswana, have undergone extensive vegetation loss and escalating heat stress despite limited economic growth (Fig. 4c). These countries are still in the early stages of urbanization, characterized by ongoing urban expansion and a decline in green and blue spaces within cities driven by economic development[39,40]. Within this context, an essential need arises to balance urbanization and vegetation preservation in these countries. Learning from more urbanized peers in the Global South can aid these countries to better navigate their urbanization trajectories to avoid negative consequences. One such valuable source of learning is China. Over recent decades, China's economic growth has outpaced the average for other Global South countries by a factor of four (Fig. 4c). Nonetheless, most urban cores in China display either greening-induced cooling or marginal warming (Fig. 3a,b). Notably, almost 60% of the Global South cities that experience greening originate from China (Supplementary Fig. 8). This success may be attributed to China's nationwide policy emphasis on safeguarding green infrastructure during urbanization[19,33]. Examples include the National Garden City program initiated in 1992 and its upgrade iterations, the 2004 National Forest City program alongside relevant regulations, the 2014 Sponge City urban planning program and the 2016 National Ecological Garden City program, which incentivize local authorities to protect and cultivate urban green spaces[41,42]. India provides another illustrative example (Fig. 4c). To promote urban green infrastructure development, India has adopted national policies such as the 2014 Urban Greening Guidelines, along with localized urban greening policies within specific cities[43]. China's and India's experience provides a blueprint for sustainable urbanization, demonstrating the feasibility of achieving economic prosperity alongside environmental stewardship[29,32]. Their lessons highlight the value of proactive planning and policymaking in preserving vegetation-induced cooling during rapid urbanization. Whereas these successful national policies may not be directly transferable to other Global South countries due to differing socio-political and economic conditions, the context-specific, nature-inspired insights from greening efforts in many Chinese and Indian cities demonstrate a valuable model of harmonious urban expansion that is both economically and environmentally sustainable. These insights can provide valuable examples for cities from other Global South countries with similar economic statuses or constrained resources (Supplementary Note 6).

Our study combined temperature and humidity to enhance the quantification of urban heat stress, following established approaches[5,13,20]. Nevertheless, a more comprehensive evaluation of heat stress necessitates the inclusion of additional environmental parameters such as radiation and wind speed[44,45]. Future studies on urban heat stress trends could leverage in situ observations and fine-resolution urban climate models to integrate these environmental variables. Furthermore, whereas the statistical isolation method for

assessing heating rates induced by vegetation loss has been widely utilized[27,28], it does not account for variations in vegetation type and structure. This limitation is particularly pertinent in the Global South, where many cities have witnessed recent expansion of rice plantations and oil palm in their urban-rural transitional zones (ref. 46; Supplementary Note 7). Future refinements may consider integrating this crucial information to provide a more comprehensive assessment of heat stress trends induced by urban browning. Additionally, the current study prioritizes interventions at national and municipal levels due to the focus on the entirety of the Global South in our analysis. Nonetheless, even within the same city, different neighborhoods may exhibit sharp thermal, socio-economic and demographic disparities[47–50]. Policymakers must acknowledge these disparities and ensure that neighborhoods with the highest vulnerability receive adequate support.

In short, our study highlights three messages. First, limitations inherent in satellite- and ground-based measurements and reanalysis data impede their capacity to accurately capture the trends in moist heat stress across heterogeneous urban landscapes. However, integrating these data sources with additional remotely sensed urban surface parameters alongside advanced machine learning techniques provides a promising solution for high-resolution mapping of such urban environmental changes, particularly for the Global South cities with limited monitoring infrastructure. Second, unlike their Global North counterparts, Global South cities encounter unique challenges in addressing urban heat stress linked to urban browning and intertwined with socio-economic realities. Given resource limitations prevalent in these countries, prioritizing cities in dire need of intervention is crucial. Third, despite diverse technological capabilities and resource availability across Global South countries, their shared historical narratives and socio-economic challenges offer opportunities for mutual learning. Inspiration and lessons from more developed peers, such as China and India, can provide precious insights into advancing urban sustainability. Such knowledge exchange is particularly valuable for the Global South as they navigate the complex challenges of extensive urbanization and rapid climate change in coming decades[6].

Methods

Study area and data

We selected 2,341 cities in the Global South, each with an urban area exceeding 10 km^2 in 2000, for our primary analysis (Fig. 2). These cities were categorized into four groups based on quartiles of urban population density (Supplementary Fig. 14): small cities (<630 persons km^{-2}), medium cities (630–1,977 persons km^{-2}), large cities (1,977–4,430 persons km^{-2}) and megacities (>4,430 persons km^{-2}). Additionally, these cities were classified into four income brackets based on GDP per capita[51], including low-income (LIC; GDP per capita < US$1,045; 19 cities), low–middle income (LMIC; US$1,045–4,125; 184 cities), upper–middle income (UMIC; US$4,126–12,735; 1,078 cities) and high-income cities (HIC; >US$12,735; 1,012 cities). We also selected 3,302 cities in the Global North for comparison, applying the same criterion of an urban area exceeding 10 km^2 in 2000.

In situ data for 2003–2020. In situ hourly surface air temperature (SAT) and relative humidity (RH) measurements were obtained from the HadISD dataset[52] and were utilized to generate 1-km urban Heat Index (HI) data. The HadISD dataset encompasses over 9,600 monitoring stations worldwide, with 2,083 in the Global South. These SAT and RH measurements are of high quality and have been widely used[4,53,54]. We first converted the universal time coordinated time to local solar time and then created composites of hourly averages for daytime (14:00–16:00) and nighttime (04:00–06:00), corresponding to the typical observation times of daily maximum and minimum SATs[55].

MODIS data for 2003–2020. We utilized MODIS data including land surface temperature (LST) from the MYD11A2 (with a temporal resolution of 8-day and spatial resolution of 1-km; ref. 56), enhanced vegetation index (EVI) from the MOD13A2 (16-day; 1-km; ref. 57), white sky albedo (WSA) from the MCD43A3 (daily; 500-m; ref. 58) and land-cover type from the MCD12Q1 (yearly; 500 m; ref. 59). The LST, EVI and WSA data were used as predictors to generate 1-km urban HI datasets. The International Geosphere Biosphere Programme classification scheme in land-cover-type data was employed to delineate urban surfaces by excluding water, permanent wetlands and snow and ice pixels[60]. To mitigate the impacts of cloud contamination, we considered only LST observations with the retrieval error of 3.0 K or less[60,61] and further applied these filtered LST pixels to mask the EVI and WSA data. The number of valid observation days for LST, EVI and WSA is presented in Supplementary Fig. 15. All datasets were resampled to 1-km resolution using the nearest neighbor method.

ERA5-Land reanalysis data for 2003–2020. We used the monthly-mean SAT, dew point temperature, precipitation and net shortwave radiation provided by the ERA5-Land Monthly Aggregated climate reanalysis dataset[62]. These data possess a spatial resolution of around 9 km, and we also resampled them to 1 km to generate urban HI datasets.

Socio-economic data for 2003–2020. We employed gridded population count (POP), GDP per capita and nighttime light (NTL) data for our analysis. The POP data at 1-km resolution are from the LandScan dataset[63]. This dataset was used to categorize city sizes based on the average urban population density from 2003 to 2020 and to generate the 1-km urban HI dataset. The 1-km GDP per capita data were sourced from the Gridded Global GDP and HDI datasets[64]. This dataset integrates both subnational and national data, thereby ensuring official statistical consistency. We employed this dataset to categorize cities into LIC, LMIC, UMIC and HIC groups according to their economic status in 2015. The 1-km NTL data obtained from the Suomi National Polar-orbiting Partnership Visible Infrared Imaging Radiometer Suite (NPP-VIIRS)-like NTL dataset[65] were also leveraged to generate urban HI datasets. This dataset was chosen due to its superior quality and enhanced detection capabilities[65], which enables more accurate monitoring of long-term socio-economic dynamics.

Urban boundary data for 2000 and 2018. We obtained the urban boundaries from the Global Urban Boundary (GUB) dataset, which maps more than 65,000 urban clusters with an area larger than 1 km^2 worldwide[66]. We utilized this dataset for consistent demarcation of urban areas. Specifically, urban surfaces are highly heterogeneous[67], with urban fringes typically demonstrating more pronounced vegetation loss than urban cores[15]. To capture this variability in urban browning and its effects on urban heat stress trends, we divided the urban surfaces into 'urban cores' (that is, urban surfaces within the GUB boundaries of 2000) and 'urban transitional zones' (that is, urban surfaces in GUB boundaries added between 2000 and 2018).

Estimation of urban heat stress trends in the Global South

We developed a multi-source data-driven model to produce high-resolution (1-km) time series data of urban heat stress for cities in the Global South, by integrating ground-based observations, satellite-derived temperatures and reanalysis data (Step 1). Subsequently, we analyzed the trends in urban heat stress and associated spatio-temporal patterns using this model-generated dataset (Step 2). Lastly, we examined the robustness of our results through comprehensive validations of both the generated urban heat stress datasets and their derived trends against the ground-based observations (Step 3).

Step 1 Generating 1-km urban HI dataset for 2003–2020 for Global South cities. We utilized the HI, as recognized by the U.S. National Oceanic and Atmospheric Administration[5,35], as our primary metric for assessing urban heat stress. Our primary analysis focused on summertime trends (June to August for Northern Hemisphere cities and

December to February for Southern Hemisphere cities) because urban residents typically encounter elevated heat stress during this period[68], but annual mean results were also provided for reference (Supplementary Fig. 16). The summertime analysis exclusively utilized data from corresponding months, whereas the annual analysis encompassed data from the entire year. Details for generating the summertime urban HI dataset are provided as the following:

(1) Quality control of in situ observations. Accurate estimation of urban heat stress hinges on high-quality in situ observations within cities. To ensure reliability, we implemented a rigorous quality control process. First, we identified 1,361 stations within 2018 urban boundaries and their 15-km buffer zones of Global South cities, labeling them, respectively, as urban and quasi-urban stations[69]. Second, for each station, we removed outliers in both SAT and RH time series using the 'three times standard deviation' rule[70]. Third, to address missing data issues, stations were evaluated based on the availability of summertime observations. Only stations with at least 45 summertime days of both SAT and RH each year were selected for synthesizing summertime average HI according to ref. 5. After this criterion, stations lacking more than 10 years of summertime HI data were excluded. This whole process led to the retention of 887 and 781 stations for estimating daytime and nighttime HI, respectively (Supplementary Fig. 17).

(2) Development of a data-driven model for urban HI mapping. We employed the Random Forest (RF) approach to develop spatio-temporal estimation models for generating 1-km resolution urban HI time series data. This approach is renowned for capturing complex nonlinear relationships and producing spatially continuous data[69]. Considering the multifaceted influences of background climate and urban-related characteristics on urban heat stress[55,69,71], we selected 13 variables for constructing the RF model. These variables included spatio-temporal geolocation (year, latitude, longitude and elevation), temperature (LST), urban surface characteristics (EVI, WSA, POP and NTL) and background climate factors (reanalysis SAT, dew point temperature, precipitation and net shortwave radiation). To capture the interannual variabilities in urban HI and ensure the fidelity of its derived long-term trends, we trained a single RF model for the entire study period (2003–2020) instead of creating separate models for each year. This strategy incorporated the 'year' variable as a predictor within the model, thereby encapsulating temporal evolution information throughout the investigation period[72,73]. Separate RF models for daytime and nighttime conditions were constructed at the site scale, with 80% of the data for training and the remaining 20% for validation. On the basis of the trained RF models and 1-km resolution predictors, we generated 1-km resolution urban HI time series data for Global South cities (Supplementary Figs. 18 and 19).

Step 2 Quantifying urban HI trends across the Global South. Utilizing the generated urban HI time series data, we quantified the urban heat stress trends (termed K_{HI}) for Global South cities, by linearly regressing the urban HI against the year. To uncover intra-city variations, we assessed the K_{HI} patterns in urban cores and transitional zones. Furthermore, we explored the K_{HI} patterns across different geographical contexts within the Global South. This includes cities spanning various subcontinents, with diverse population densities and economic statuses (indicated by GDP per capita). Comparative analyses were also conducted among urban warming rates quantified using different temperature metrics: SAT, LST and HI.

Step 3 Validating urban HI and its trends. We conducted a comprehensive validation of our urban HI dataset across Global South cities and various subcontinents (Supplementary Figs. 20–23), focusing on two key aspects: absolute HI values and their temporal trends (K_{HI}). This validation process involved calculating four error metrics—correlation coefficient (R), root mean square error, mean absolute error and bias—by comparing observed and estimated values. For absolute urban HI, we used the remaining 20% in situ observation records for validation (that is, 3,273 and 2,765 for daytime and nighttime). For K_{HI}, we utilized urban stations with complete records across all years for validation (that is, 553 and 366 stations for daytime and nighttime). As detailed in Supplementary Note 1, the R values for absolute HI are 0.98 (daytime) and 0.99 (nighttime), whereas they are 0.83 (daytime) and 0.73 (nighttime) for K_{HI}. These high correlations, together with the results of root mean square errors and mean absolute errors, affirm the robustness of our generated urban HI dataset in characterizing both absolute urban HI and its derived trends.

Clarifications and uncertainty analysis. Our urban HI dataset presents distinct advantages over existing temperature datasets[24,71,74]: prioritizing heat stress, achieving high resolution (1 km) based on the selection of pertinent urban stations and emphasizing trend accuracy. First, unlike previous studies that targeted LST or SAT[71,74], our present study focuses explicitly on urban HI for the assessment of urban thermal heat stress. This distinction is particularly critical for tropical and subtropical cities in the Global South, given their inherent high humidity levels[2]. Second, earlier temperature or heat stress datasets often struggle to capture the nuanced heterogeneity of urban landscapes, either due to relatively coarse spatial resolutions[24] or substantial reliance on rural ground-based observations for calibration[72]. In contrast, our approach achieves relatively finer spatial resolution (that is, 1 km) and accurately portrays urban thermal environments by carefully selecting urban stations based on their locations and data quality. Third, existing temperature products have prioritized absolute accuracy and spatial coverage[71] while neglecting temporal consistency, which hinders accurate analysis of urban warming trends. In contrast, our urban HI dataset places equal emphasis on both absolute and trend accuracy, enabling accurate monitoring of long-term dynamics in urban thermal environments.

We acknowledge that our generated urban HI dataset may be influenced by the relatively limited number of urban stations employed for constructing RF estimation models. We thus further incorporated the Berkeley Earth dataset that provides a notably denser collection of ground-based observations for sensitivity analysis (Supplementary Note 2). The substantial agreement between the results derived from these two datasets (that is, HadISD and Berkeley) emphasizes the strong representativeness of our used urban stations and the high accuracy of the generated urban HI dataset (Supplementary Fig. 24). Moreover, recognizing that different indices have varying sensitivities to humidity and air temperature[75], we examined the potential influence of index choice on assessing urban heat stress trends. This examination involved selecting two additional heat indexes for comparative analyses: the Wet-Bulb Globe Temperature in shade conditions at stable wind (that is, indoor WBGT) and the Humidex as recommended by the Meteorological Service of Canada (Supplementary Note 3). We first generated 1-km urban time series datasets for both indoor WBGT and Humidex to parallel our HI dataset and then quantified urban heat stress trends using these alternative indices. The results indicated that although there were numerical differences in trends across these indices (that is, HI, indoor WBGT and Humidex), their spatial patterns largely align, strongly reinforcing the reliability of our primary conclusions (Supplementary Figs. 3 and 25 and Supplementary Note 3).

Evaluation of browning effects on urban heat stress trends

Urban heat stress trends result from a multifaceted interplay of background climate change (BCC), urban greenness change (UGC) and urbanization processes (URB)[15,55,76]. Disentangling these intertwined factors presents considerable challenges. Previous studies

have introduced two effective methodologies to isolate the individual contributions of these factors, that is, the spatial reference method and the space-for-time substitution strategy[15,18,77,78]. The spatial reference method heavily relies on stable vegetation cover in available reference pixels[79], a resource that may be scarce in rapidly urbanizing areas. Given this limitation, we adopted the space-for-time method to isolate the individual contributions of BCC, UGC and URB[77,80]. This strategy utilizes the least square-based statistical method[27,28] to decompose the yearly changes in urban HI into contributions from BCC, UGC and URB. Each city's HI change was modeled as a linear combination of these factors, as given by equation (1):

$$\Delta HI = \varepsilon_{BCC} \times \Delta HI_{BCC} + \varepsilon_{URB} \times \Delta HI_{URB} + \varepsilon_{UGC} \times \Delta HI_{UGC} + \varepsilon_4 \quad (1)$$

where ΔHI denotes the yearly changes in urban HI (that is, the difference in urban HI between a certain year and its previous year) for a given city; ΔHI_{BCC}, ΔHI_{URB} and ΔHI_{UGC} denote the ΔHI attributed to BCC, URB and UGC factors, respectively; ε_{BCC}, ε_{URB} and ε_{UGC} are the corresponding scale factors; and ε_4 is the residual error term.

For each city, the ΔHI_{BCC} was directly estimated using the yearly changes in rural HI derived from ERA5-Land reanalysis data. We defined the rural surroundings as the region between the 10-km and 100-km buffers outside the urban boundary in 2018 (ref. 81). The ΔHI_{URB} was characterized using the change in urban population density (POP) and was quantified with the space-for-time strategy[69,80]. We first established a linear relationship between the yearly urban HI changes and POP changes (denoted by the logarithm of POP) throughout the study period, using all pixels within the urban boundary. The ΔHI_{URB} was then determined based on this linear relationship and city-level urban POP changes each year. The ΔHI_{UGC} was also quantified using the space-for-time method. For each city, we first established a linear relationship between the yearly HI and EVI changes throughout the study period using all pixels in the rural surroundings. Subsequently, the ΔHI_{UGC} was calculated based on this relationship and city-level EVI changes each year. The HI-EVI relationship was derived from rural surfaces, primarily because urban HI is influenced by both URB and UGC factors, complicating the accurate differentiation of their individual contributions[19]. In contrast, rural surroundings, being farther from urban surfaces, may be less affected by urbanization[18]. Thus, the HI-EVI relationship derived from rural surfaces can effectively alleviate the confounding effects of urbanization, enabling a more accurate estimation of ΔHI_{UGC}. We recognize that applying the rural-based relationship to urban surfaces may introduce potential uncertainties due to the distinct factors influencing urban and rural greenness. Further discussion on this issue is provided in Supplementary Note 7.

Subsequently, we used the least square regression method to determine the scale factors (ε_{BCC}, ε_{URB} and ε_{UGC}) and the residual term (ε_4) for each city. The urban HI trends attributable to BCC, URB and UGC were then estimated. We primarily focused on the UGC-induced variations in urban HI trends (termed β_{HI}; Fig. 3 and Supplementary Fig. 26), calculated using equation (2):

$$\beta_{HI} = K_{HI} \times \frac{|\varepsilon_{UGC} \times \Delta HI_{UGC}|}{|\varepsilon_{BCC} \times \Delta HI_{BCC}| + |\varepsilon_{URB} \times \Delta HI_{URB}| + |\varepsilon_{UGC} \times \Delta HI_{UGC}| + |\varepsilon_4|} \quad (2)$$

where K_{HI} denotes urban HI trends.

Identifying cities deserving the most urgent intervention

Variations in urban HI (β_{HI}) induced by vegetation loss across Global South cities are associated with intricate physical and socio-economic interactions[82]. Considering the resource and technology constraints in these regions[6,7], it is imperative to prioritize cities that require urgent intervention. Accordingly, our study examined the correlations between β_{HI} and various physical, physiological and socio-economic indicators to identify cities in dire need of action. This was achieved using four-quadrant plots of β_{HI} against each indicator, with quadrant thresholds determined by their mean values across all countries (Supplementary Tables 1–3). It is crucial to emphasize that whereas our focus mainly rests on high-risk case cities, this does not diminish the importance of addressing vulnerabilities in other cities.

From a physical perspective, β_{HI} is closely linked to the magnitude of urban browning (K_{EVI}). However, a simplistic linear correlation between β_{HI} and K_{EVI} does not suffice due to the complex sensitivity of heat stress to vegetation loss. To decipher this intricacy across Global South cities, we analyzed country-level relationships between β_{HI} and K_{EVI} (Supplementary Table 1), identifying two distinct clusters (Supplementary Note 8). (1) Countries with low sensitivity of heat stress trends to browning, indicated by higher K_{EVI} but relatively lower β_{HI}. (2) Countries with high sensitivity of heat stress trends to browning, evidenced by lower K_{EVI} yet relatively higher β_{HI}. Cities in the latter cluster of countries necessitate imperative interventions to manage vegetation loss for mitigating heat stress.

From a physiological viewpoint, many cities in the Global South are nearing human tolerance limits with their baseline HI values[3] (Supplementary Fig. 27). In these contexts, a minor increase in β_{HI} can dramatically exacerbate extreme weather events and heat-related health impacts[83]. To contextualize the β_{HI} values within specific climatic background of each city, we assessed the relationship between β_{HI} and the absolute baseline urban HI at the country level (Supplementary Table 2). This analysis yielded a distinct category of countries with both higher β_{HI} and baseline urban HI values (Supplementary Note 8). For cities within this category of countries, even a minor rise in β_{HI} can result in a substantial surge in heat stress, highlighting the need for urgent interventions to prevent reaching a thermal tipping point.

From a socio-economic standpoint, browning-induced variations in urban HI (β_{HI}) are probably linked to economic development associated with urbanization. We examined the country-level relationship between β_{HI} and urban economic growth (measured by the percentage increase in per capita GDP throughout the study period) to guide targeted interventions (Supplementary Table 3). This analysis yielded two pivotal categories of countries (Supplementary Note 8): those with slower economic growth but larger β_{HI} and those experiencing rapid economic growth but modest β_{HI}. The former requires immediate action to reduce β_{HI} through improved urban planning, whereas the latter provides valuable insights into balancing economic development and thermal environmental degradation.

Reporting summary

Further information on research design is available in the Nature Portfolio Reporting Summary linked to this article.

Data availability

In situ hourly surface air temperature and relative humidity measurements provided by the HadISD dataset are available at https://www.metoffice.gov.uk/hadobs/hadisd/v341_202403p/download.html. In situ monthly surface air temperatures obtained from the Berkeley Earth dataset are available at https://berkeleyearth.org/data/. The land surface temperature data from the MYD11A2 product are available at https://developers.google.cn/earth-engine/datasets/catalog/MODIS_061_MYD11A2. The enhanced vegetation index data from the MOD13A2 product are available at https://developers.google.cn/earth-engine/datasets/catalog/MODIS_061_MOD13A2. The white sky albedo data from the MCD43A3 product are available at https://developers.google.cn/earth-engine/datasets/catalog/MODIS_061_MCD43A3. The land-cover-type data from the MCD12Q1 product are available at https://developers.google.cn/earth-engine/datasets/catalog/MODIS_061_MCD12Q1. The ERA5-Land Monthly Aggregated climate reanalysis dataset is available at https://developers.google.cn/earth-engine/datasets/catalog/ECMWF_ERA5_LAND_MONTHLY_AGGR.

The gridded population count data from the LandScan dataset are available at https://developers.google.com/earth-engine/datasets/catalog/projects_sat-io_open-datasets_ORNL_LANDSCAN_GLOBAL. The GDP per capita data from the Gridded Global GDP and HDI datasets are available at https://gee-community-catalog.org/projects/gridded_gdp_hdi/. The global urban boundary dataset is available at https://data-starcloud.pcl.ac.cn/zh/resource/14. The global administrative boundary data are available at https://gadm.org/download_world.html.

Code availability

The analysis was primarily conducted using the Google Earth Engine platform (https://code.earthengine.google.com/), Python (Version 3.8) and MATLAB (Version R2019a). The random forest algorithm was performed on the Google Earth Engine platform. All the necessary codes can be accessed through GitHub (https://github.com/HuilinDu/GS_UrbanHeating). For assistance with executing the codes, please contact the corresponding authors.

References

1. United Nations. World urbanization prospects: the 2018 revision *UN DESA* http://esa.un.org/unpd/wup/ (2018).
2. Agarwal, N., Nagpure, A. & Ramaswami, A. Studying extreme heat and social inequality in global south cities: recommendations for cross-cultural research. *One Earth* **7**, 1324–1329 (2024).
3. Andrews, O., Le Quere, C., Kjellstrom, T., Lemke, B. & Haines, A. Implications for workability and survivability in populations exposed to extreme heat under climate change: a modelling study. *Lancet Planet. Health* **2**, e540–e547 (2018).
4. Raymond, C., Matthews, T. & Horton, R. M. The emergence of heat and humidity too severe for human tolerance. *Sci. Adv.* **6**, eaaw1838 (2020).
5. Tuholske, C. et al. Global urban population exposure to extreme heat. *Proc. Natl Acad. Sci. USA* **118**, e2024792118 (2021).
6. IPCC. *Climate Change 2022: Impacts, Adaptation, and Vulnerability* (eds Pörtner, H.-O. et al.) (Cambridge Univ. Press, 2022).
7. Virgüez, E., Leon, L. & Freese, L. M. The climate sciences need representation from the global south. *One Earth* **7**, 370–373 (2024).
8. Zhang, W. M. et al. Socio-economic and climatic changes lead to contrasting global urban vegetation trends. *Glob. Environ. Change* **71**, 102385 (2021).
9. Kephart, J. L. et al. City-level impact of extreme temperatures and mortality in Latin America. *Nat. Med.* **28**, 1700–1705 (2022).
10. Hamdi, R. et al. The state-of-the-art of urban climate change modeling and observations. *Earth Syst. Environ.* **4**, 631–646 (2020).
11. Varquez, A. C. & Kanda, M. Global urban climatology: a meta-analysis of air temperature trends (1960–2009). *npj Clim. Atmos. Sci.* **1**, 32 (2018).
12. Wang, W. & Shu, J. Urban renewal can mitigate urban heat islands. *Geophys. Res. Lett.* **47**, e2019GL085948 (2020).
13. Luo, M. & Lau, N. C. Increasing human-perceived heat stress risks exacerbated by urbanization in China: a comparative study based on multiple metrics. *Earth's Future* **9**, e2020EF001848 (2021).
14. Li, Z. L. et al. Satellite remote sensing of global land surface temperature: definition, methods, products, and applications. *Rev. Geophys.* **61**, e2022RG000777 (2023).
15. Liu, Z. H. et al. Surface warming in global cities is substantially more rapid than in rural background areas. *Commun. Earth Environ.* **3**, 219 (2022).
16. Ju, Y., Dronova, I., Rodriguez, D. A., Bakhtsiyarava, M. & Farah, I. Recent greening may curb urban warming in Latin American cities of better economic conditions. *Landscape Urban Plann.* **240**, 104896 (2023).
17. Sethi, S. S. & Vinoj, V. Urbanization and regional climate change-linked warming of Indian cities. *Nat. Cities* **1**, 402–405 (2024).
18. Li, L. et al. Competition between biogeochemical drivers and land-cover changes determines urban greening or browning. *Remote Sens. Environ.* **287**, 113481 (2023).
19. Xu, D. et al. Reassessing the climate mitigation potential of Chinese ecological restoration: the undiscovered potential of urban areas. *Innovation Geosci.* **2**, 100068 (2024).
20. Chakraborty, T. C., Venter, Z. S., Qian, Y. & Lee, X. H. Lower urban humidity moderates outdoor heat stress. *AGU Adv.* **3**, e2022AV000729 (2022).
21. Chakraborty, T. C., Newman, A. J., Qian, Y., Hsu, A. & Sheriff, G. Residential segregation and outdoor urban moist heat stress disparities in the United States. *One Earth* **6**, 738–750 (2023).
22. Kelly Turner, V. et al. More than surface temperature: mitigating thermal exposure in hyper-local land system. *J. Land Use Sci.* **17**, 79–99 (2022).
23. Lee, J. & Dessler, A. E. Improved surface urban heat impact assessment using GOES satellite data: a comparative study with ERA-5. *Geophys. Res. Lett.* **51**, e2023GL107364 (2024).
24. Verdin, A. et al. Development and validation of the CHIRTS-daily quasi-global high-resolution daily temperature data set. *Sci. Data* **7**, 303 (2020).
25. Krayenhoff, E. S. et al. Cooling hot cities: a systematic and critical review of the numerical modelling literature. *Environ. Res. Lett.* **16**, 053007 (2021).
26. Sherwood, S. C. How important is humidity in heat stress? *J. Geophys. Res. Atmos.* **123**, 11808–11810 (2018).
27. Hegerl, G. C. et al. Multi-fingerprint detection and attribution analysis of greenhouse gas, greenhouse gas-plus-aerosol and solar forced climate change. *Clim. Dyn.* **13**, 613–634 (1997).
28. Sun, Y., Zhang, X. B., Ren, G. Y., Zwiers, F. W. & Hu, T. Contribution of urbanization to warming in China. *Nat. Clim. Change* **6**, 706–709 (2016).
29. Sun, L. Q., Chen, J., Li, Q. L. & Huang, D. Dramatic uneven urbanization of large cities throughout the world in recent decades. *Nat. Commun.* **11**, 5366 (2020).
30. Awuni, S. et al. Managing the challenges of climate change mitigation and adaptation strategies in Ghana. *Heliyon* **9**, e15491 (2023).
31. Shackleton, S., Ziervogel, G., Sallu, S., Gill, T. & Tschakert, P. Why is socially-just climate change adaptation in sub-Saharan Africa so challenging? A review of barriers identified from empirical cases. *Wiley Interdiscip. Rev. Clim. Change* **6**, 321–344 (2015).
32. Lu, Y. L. et al. Forty years of reform and opening up: China's progress toward a sustainable path. *Sci. Adv.* **5**, eaau9413 (2019).
33. Feng, D. R., Bao, W. K., Yang, Y. Y. & Fu, M. C. How do government policies promote greening? Evidence from China. *Land Use Policy* **104**, 105389 (2021).
34. Randolph, G. F. & Storper, M. Is urbanisation in the global south fundamentally different? Comparative global urban analysis for the 21st century. *Urban Stud.* **60**, 3–25 (2022).
35. What is the heat index? *NOAA* https://www.weather.gov/ama/heatindex (2012).
36. Yang, Q. Q. et al. Global assessment of urban trees' cooling efficiency based on satellite observations. *Environ. Res. Lett.* **17**, 034029 (2022).
37. Haaland, C. & van Den Bosch, C. K. Challenges and strategies for urban green-space planning in cities undergoing densification: a review. *Urban For. Urban Greening* **14**, 760–771 (2015).
38. Liberalesso, T., Cruz, C. O., Silva, C. M. & Manso, M. Green infrastructure and public policies: an international review of green roofs and green walls incentives. *Land Use Policy* **96**, 104693 (2020).

39. Fall, M. & Coulibaly, S. *Diversified Urbanization: The Case of Côte d'Ivoire* (World Bank Publications, 2016).
40. Gwebu, T. D. Policy implications of urbanisation patterns and processes in Botswana. *Botswana Notes Rec.* **46**, 84–98 (2014).
41. Nguyen, T. T. et al. Implementation of a specific urban water management—Sponge City. *Sci. Total Environ.* **652**, 147–162 (2019).
42. Zhang, Y. J., Zhang, T. Z., Zeng, Y. X., Cheng, B. D. & Li, H. X. Designating national forest cities in China: does the policy improve the urban living environment? *Forest Policy Econ.* **125**, 102400 (2021).
43. Imam, A. U. & Banerjee, U. K. Urbanisation and greening of Indian cities: problems, practices, and policies. *Ambio* **45**, 442–457 (2016).
44. Blazejczyk, K., Epstein, Y., Jendritzky, G., Staiger, H. & Tinz, B. Comparison of UTCI to selected thermal indices. *Int. J. Biometeorol.* **56**, 515–535 (2012).
45. Middel, A., Lukasczyk, J. & Maciejewski, R. Sky view factors from synthetic fisheye photos for thermal comfort routing—a case study in Phoenix, Arizona. *Urban Plann.* **2**, 19–30 (2017).
46. Xu, Y. D. et al. Recent expansion of oil palm plantations into carbon-rich forests. *Nat. Sustain.* **5**, 574–577 (2022).
47. Chen, B. et al. Contrasting inequality in human exposure to greenspace between cities of global north and global south. *Nat. Commun.* **13**, 4636 (2022).
48. Hsu, A., Sheriff, G., Chakraborty, T. & Manya, D. Disproportionate exposure to urban heat island intensity across major US cities. *Nat. Commun.* **12**, 2721 (2021).
49. Rocha, A. D. et al. Unprivileged groups are less served by green cooling services in major European urban areas. *Nat. Cities* **1**, 424–435 (2024).
50. Yin, Y., He, L. Y., Wennberg, P. O. & Frankenberg, C. Unequal exposure to heatwaves in Los Angeles: impact of uneven green spaces. *Sci. Adv.* **9**, eade8501 (2023).
51. New World Bank country classifications by income level: 2022–2023. *World Bank* https://datahelpdesk.worldbank.org/knowledgebase/articles/906519-world-bank-country-and-lending-groups (2022).
52. Dunn, R. J., Willett, K. M., Parker, D. E. & Mitchell, L. Expanding HadISD: quality-controlled, sub-daily station data from 1931. *Geosci. Instrum. Methods Data Syst.* **5**, 473–491 (2016).
53. Dong, J. Q., Brönnimann, S., Hu, T., Liu, Y. X. & Peng, J. GSDM-WBT: global station-based daily maximum wet-bulb temperature data for 1981–2020. *Earth Syst. Sci. Data* **14**, 5651–5664 (2022).
54. Meili, N., Paschalis, A., Manoli, G. & Fatichi, S. Diurnal and seasonal patterns of global urban dry islands. *Environ. Res. Lett.* **17**, 054044 (2022).
55. Oke, T. R., Mills, G., Christen, A. & Voogt, J. A. *Urban Climates* (Cambridge Univ. Press, 2017).
56. Wan, Z. M. *Collection-6 MODIS Land Surface Temperature Products Users' Guide* (Univ. of California, 2013).
57. Didan, K., Munoz, A. B., Solano, R. & Huete, A. *MODIS Vegetation Index User's Guide (MOD13 Series)* (Univ. of Arizona: Vegetation Index and Phenology Lab, 2015).
58. Wang, D. D. et al. Estimating daily mean land surface albedo from MODIS data. *J. Geophys. Res. Atmos.* **120**, 4825–4841 (2015).
59. Friedl, M. & Sulla-Menashe, D. MCD12Q1 MODIS/Terra+ Aqua land cover type yearly L3 global 500 m SIN grid V006. *NASA EOSDIS Land Processes DAAC* **10**, 200 (2019).
60. Venter, Z. S., Chakraborty, T. & Lee, X. H. Crowdsourced air temperatures contrast satellite measures of the urban heat island and its mechanisms. *Sci. Adv.* **7**, eabb9569 (2021).
61. Chakraborty, T. & Qian, Y. Urbanization exacerbates continental-to regional-scale warming. *One Earth* **7**, 1387–1401 (2024).
62. Muñoz-Sabater, J. *ERA5-Land Monthly Averaged Data from 1981 to Present* (Copernicus Climate Change Service Climate Data Store, 2019). https://cds.climate.copernicus.eu/datasets/reanalysis-era5-land-monthly-means?tab=overview
63. Sims, K., Reith, A., Bright, E., McKee, J. & Rose, A. LandScan Global 2021. *Oak Ridge National Laboratory* https://landscan.ornl.gov/ (2022).
64. Kummu, M., Taka, M. & Guillaume, J. H. A. Gridded global datasets for gross domestic product and human development index over 1990–2015. *Sci. Data* **5**, 180004 (2018).
65. Chen, Z. Q. et al. An extended time series (2000–2018) of global NPP-VIIRS-like nighttime light data from a cross-sensor calibration. *Earth Syst. Sci. Data* **13**, 889–906 (2021).
66. Li, X. C. et al. Mapping global urban boundaries from the global artificial impervious area (GAIA) data. *Environ. Res. Lett.* **15**, 094044 (2020).
67. Stewart, I. D. & Oke, T. R. Local climate zones for urban temperature studies. *Bull. Amer. Meteorol. Soc.* **93**, 1879–1900 (2012).
68. Zhang, K. E. et al. Increased heat risk in wet climate induced by urban humid heat. *Nature* **617**, 738–742 (2023).
69. Li, J. F. et al. Satellite-based ranking of the world's hottest and coldest cities reveals inequitable distribution of temperature extremes. *Bull. Amer. Meteorol. Soc.* **104**, E1268–E1281 (2023).
70. Li, L. et al. Long-term and fine-scale surface urban heat island dynamics revealed by Landsat data since the 1980s: a comparison of four megacities in China. *J. Geophys. Res. Atmos.* **127**, e2021JD035598 (2022).
71. Zhang, T. et al. A global dataset of daily maximum and minimum near-surface air temperature at 1 km resolution over land (2003–2020). *Earth Syst. Sci. Data* **14**, 5637–5649 (2022).
72. Yang, Z. W. et al. GloUTCI-M: a global monthly 1 km universal thermal climate index dataset from 2000 to 2022. *Earth Syst. Sci. Data* **16**, 2407–2424 (2024).
73. Zhang, H. et al. HiTIC-Monthly: a monthly high spatial resolution (1 km) human thermal index collection over China during 2003–2020. *Earth Syst. Sci. Data* **15**, 359–381 (2023).
74. Hooker, J., Duveiller, G. & Cescatti, A. A global dataset of air temperature derived from satellite remote sensing and weather stations. *Sci. Data* **5**, 180246 (2018).
75. Simpson, C. H., Brousse, O., Ebi, K. L. & Heaviside, C. Commonly used indices disagree about the effect of moisture on heat stress. *npj Clim. Atmos. Sci.* **6**, 78 (2023).
76. Du, H. L. et al. Contrasting trends and drivers of global surface and canopy urban heat islands. *Geophys. Res. Lett.* **50**, e2023GL104661 (2023).
77. Li, J. F. et al. Similarities and disparities in urban local heat islands responsive to regular-, stable-, and counter-urbanization: a case study of Guangzhou, China. *Build. Environ.* **199**, 107935 (2021).
78. Li, Y. T. et al. Biophysical impacts of earth greening can substantially mitigate regional land surface temperature warming. *Nat. Commun.* **14**, 121 (2023).
79. Yao, R., Wang, L. C., Huang, X., Gong, W. & Xia, X. G. Greening in rural areas increases the surface urban heat island intensity. *Geophys. Res. Lett.* **46**, 2204–2212 (2019).
80. Pickett, S. T. in *Long-Term Studies in Ecology: Approaches and Alternatives* 110–135 (Springer, 1989).
81. Luo, M. & Lau, N. C. Increasing heat stress in urban areas of eastern China: acceleration by urbanization. *Geophys. Res. Lett.* **45**, 13,060–13,069 (2018).
82. Hartinger, S. M. et al. The 2022 South America report of The Lancet Countdown on health and climate change: trust the science. Now that we know, we must act. *Lancet Reg. Health–Americas* **20**, 100470 (2023).

83. Zhao, L. et al. Global multi-model projections of local urban climates. *Nat. Clim. Change* **11**, 152–157 (2021).

Acknowledgements

This study was supported by the National Natural Science Foundation of China under grant number 423B2105 (H.D.), the Fundamental Research Funds for the Central Universities under grant number 2024300388 (W.Z.) and the Fundamental Research Funds for the Central Universities—Cemac 'GeoX' Interdisciplinary Program under grant number 020714380210 (W.Z.). This study was also supported by the National Natural Science Foundation of China under grant numbers 42171306 (W.Z.) and 42201337 (Z.L.). We also thank the support from the National Youth Talent Support Program of China (W.Z.). T.C.'s contribution was supported by the US Department of Energy, Office of Science, Biological and Environmental Research program through the Early Career Research Program. Pacific Northwest National Laboratory is operated for DOE by Battelle Memorial Institute under contract DEAC05-76RL01830.

Author contributions

W.Z. conceived and designed the research; H.D. and W.Z. performed data analysis; H.D. and W.Z. wrote the manuscript; and B.Z., Y. Ju, Z.L., A.M., K.H., L.Z., T.C., Z.W., S.W., J.L., L.L., F.H., Y. Ji, X.L. and M.L. contributed ideas to data analysis, interpretation of results or manuscript revisions.

Competing interests

The authors declare no competing interests.

Additional information

Supplementary information The online version contains supplementary material available at https://doi.org/10.1038/s44284-024-00184-9.

Correspondence and requests for materials should be addressed to Wenfeng Zhan or Manchun Li.

Peer review information *Nature Cities* thanks Josiah Kephart and the other, anonymous, reviewer(s) for their contribution to the peer review of this work.

nature portfolio

Corresponding author(s): Wenfeng Zhan

Last updated by author(s): Oct 21, 2024

Reporting Summary

Nature Portfolio wishes to improve the reproducibility of the work that we publish. This form provides structure for consistency and transparency in reporting. For further information on Nature Portfolio policies, see our Editorial Policies and the Editorial Policy Checklist.

Statistics

For all statistical analyses, confirm that the following items are present in the figure legend, table legend, main text, or Methods section.

n/a	Confirmed	
☐	☒	The exact sample size (*n*) for each experimental group/condition, given as a discrete number and unit of measurement
☐	☒	A statement on whether measurements were taken from distinct samples or whether the same sample was measured repeatedly
☐	☒	The statistical test(s) used AND whether they are one- or two-sided *Only common tests should be described solely by name; describe more complex techniques in the Methods section.*
☒	☐	A description of all covariates tested
☐	☒	A description of any assumptions or corrections, such as tests of normality and adjustment for multiple comparisons
☐	☒	A full description of the statistical parameters including central tendency (e.g. means) or other basic estimates (e.g. regression coefficient) AND variation (e.g. standard deviation) or associated estimates of uncertainty (e.g. confidence intervals)
☐	☒	For null hypothesis testing, the test statistic (e.g. *F*, *t*, *r*) with confidence intervals, effect sizes, degrees of freedom and *P* value noted *Give P values as exact values whenever suitable.*
☒	☐	For Bayesian analysis, information on the choice of priors and Markov chain Monte Carlo settings
☒	☐	For hierarchical and complex designs, identification of the appropriate level for tests and full reporting of outcomes
☒	☐	Estimates of effect sizes (e.g. Cohen's *d*, Pearson's *r*), indicating how they were calculated

Our web collection on statistics for biologists contains articles on many of the points above.

Software and code

Policy information about availability of computer code

Data collection	All the datasets used in this study were freely downloaded from official website and no software was used.
Data analysis	Google Earth Engine (GEE) Cloud Platform (https://code.earthengine.google.com/), Python 3.8, and Matlab R 2019a were mainly used for data analysis in this study. The random forest algorithm was performed on the GEE platform. All the necessary codes can be accessed through GitHub (https://github.com/HuilinDu/GS_UrbanHeating).

For manuscripts utilizing custom algorithms or software that are central to the research but not yet described in published literature, software must be made available to editors and reviewers. We strongly encourage code deposition in a community repository (e.g. GitHub). See the Nature Portfolio guidelines for submitting code & software for further information.

Data

Policy information about availability of data

All manuscripts must include a data availability statement. This statement should provide the following information, where applicable:

- Accession codes, unique identifiers, or web links for publicly available datasets
- A description of any restrictions on data availability
- For clinical datasets or third party data, please ensure that the statement adheres to our policy

In-situ hourly surface air temperature and relative humidity measurements provided by the HadISD dataset are available at https://www.metoffice.gov.uk/hadobs/hadisd/v341_202403p/download.html. In-situ monthly surface air temperatures obtained from the Berkeley Earth dataset are available at https://

berkeleyearth.org/data/. The land surface temperature data from the MYD11A2 product are available https://developers.google.cn/earth-engine/datasets/catalog/MODIS_061_MYD11A2. The enhanced vegetation index data from the MOD13A2 product are available at https://developers.google.cn/earth-engine/datasets/catalog/MODIS_061_MOD13A2. The white sky albedo data from the MCD43A3 product are available at https://developers.google.cn/earth-engine/datasets/catalog/MODIS_061_MCD43A3. The land cover type data from the MCD12Q1 product are available at https://developers.google.cn/earth-engine/datasets/catalog/MODIS_061_MCD12Q1. The ERA5-Land Monthly Aggregated climate reanalysis dataset is available at https://developers.google.cn/earth-engine/datasets/catalog/ECMWF_ERA5_LAND_MONTHLY_AGGR. The gridded population count data from the LandScan dataset are available at https://developers.google.com/earth-engine/datasets/catalog/projects_sat-io_open-datasets_ORNL_LANDSCAN_GLOBAL. The GDP per capita data from the Gridded Global GDP and HDI datasets are available at https://gee-community-catalog.org/projects/gridded_gdp_hdi/. The global urban boundary dataset is available at https://data-starcloud.pcl.ac.cn/zh/resource/14.

Human research participants

Policy information about studies involving human research participants and Sex and Gender in Research.

Reporting on sex and gender	Sex and gender were not considered in this study.
Population characteristics	Human research participants were not involved in this study.
Recruitment	None.
Ethics oversight	None.

Note that full information on the approval of the study protocol must also be provided in the manuscript.

Field-specific reporting

Please select the one below that is the best fit for your research. If you are not sure, read the appropriate sections before making your selection.

☐ Life sciences ☐ Behavioural & social sciences ☒ Ecological, evolutionary & environmental sciences

For a reference copy of the document with all sections, see nature.com/documents/nr-reporting-summary-flat.pdf

Ecological, evolutionary & environmental sciences study design

All studies must disclose on these points even when the disclosure is negative.

Study description	Our current study, employing a novel methodological approach and a comparative spatial perspective, offers critical insights into the spatiotemporal patterns of urban heat stress trends, the influence of urban browning, and their broader implications for urban governance and sustainability within the Global South.
Research sample	This study selected 2,341 cities in the Global South for analysis.
Sampling strategy	Across the Global South, all cities with an urban area exceeding 10 km2 in 2000 were selected by us according to the Global Boundary Dataset. These selected cities span various sub-continents, diverse population sizes, as well as different economic statuses.
Data collection	All the MODIS products, reanalysis materials, and socioeconomic data are publicly available on the Google Earth Engine (GEE) platform (https://developers.google.cn/earth-engine/datasets/catalog/). The global urban boundary dataset is available at https://data-starcloud.pcl.ac.cn/zh/resource/14. The in-situ hourly surface air temperature and relative humidity measurements are available at https://www.metoffice.gov.uk/hadobs/hadisd/v341_202403p/download.html, and those monthly surface air temperatures are available at https://berkeleyearth.org/data/.
Timing and spatial scale	Timing scale: summertime during the period 2003 to 2020; Spatial scale: 2,341 cities in the Global South.
Data exclusions	No data were excluded from the analysis
Reproducibility	All attempts to repeat the experiment were successful.
Randomization	The chosen 2,341 cities in the Global South were allocated by continent and climate zone. This allocation strategy is very common and well accepted in urban studies across the globe.
Blinding	Blinding is not relevant to our study because no recruitment of participant is necessary for our study.

Did the study involve field work? ☐ Yes ☒ No

Reporting for specific materials, systems and methods

We require information from authors about some types of materials, experimental systems and methods used in many studies. Here, indicate whether each material, system or method listed is relevant to your study. If you are not sure if a list item applies to your research, read the appropriate section before selecting a response.

Materials & experimental systems

n/a	Involved in the study
☒	☐ Antibodies
☒	☐ Eukaryotic cell lines
☒	☐ Palaeontology and archaeology
☒	☐ Animals and other organisms
☒	☐ Clinical data
☒	☐ Dual use research of concern

Methods

n/a	Involved in the study
☒	☐ ChIP-seq
☒	☐ Flow cytometry
☒	☐ MRI-based neuroimaging